Supplemental Material for
High-Temperature Charge-Stripe Correlations in $La_{1.675}Eu_{0.2}Sr_{0.125}CuO_4$

Q. Wang *et al.*

I. SCATTERING GEOMETRY AND RIXS CROSS-SECTION

The scattering geometry of the RIXS experiments are given in Fig. 1(c) and Table S1. At certain photon energy, the magnitude of total momentum transfer $|\mathbf{Q}|$ is determined by the scattering angle γ. By changing the incident angle θ and sample azimuthal angle ϕ, the in-plane component $\mathbf{Q}_{\parallel}$ can be varied. The range of ℓ covered in each measurement and the value (ℓ_0) at the in-plane charge ordering wavevector at base temperature are shown in Table S1.

The RIXS intensity (proportional to cross-section) from initial state $|i\rangle$ to final state $|f\rangle$ can be expressed by the Kramers-Heisenberg equation [1]:

$$I_{fi}(\epsilon,\epsilon') \propto \left| \sum_n \frac{\left\langle f \left| D^{\dagger}_{\epsilon'} \right| n \right\rangle \langle n | D_{\epsilon} | i \rangle}{E_i - E_n + \hbar\omega_k + i\Gamma_n/2} \right|^2 \delta\left(E_i - E_f + \hbar\omega_k - \hbar\omega'_k\right) \tag{1}$$

where ω_k, ϵ (ω'_k, ϵ') are the energy and momentum of the incident (scattered) photon. D_ϵ ($D_{\epsilon'}$) is the polarization dependent dipole operator. E_i, E_f and E_n are the energy of initial, final and intermediate state $|n\rangle$. Γ_n is the inverse core-hole lifetime. The resonant scattering is enhanced when the incident photon is in resonance with a specific transition in the sample *i.e.* $\hbar\omega_k \approx E_n - E_i$.

In the case of scattering from charge order, the RIXS intensity is dominated by the polarization preserving elastic scattering processes ($\sigma \to \sigma$, $\pi \to \pi$). Under the single ion approximation, we obtain the amplitude for such scattering with σ and π polarized incident x-ray [2, 3]:

$$I(\sigma,\sigma) = I_0[1 + \frac{1}{4}\sin^2(\alpha - \frac{\gamma}{2})\cos^2\theta_{\text{spin}}] \tag{2}$$

$$I(\pi,\pi) = I_0 \sin^2(\alpha + \frac{\gamma}{2})[\sin^2(\alpha - \frac{\gamma}{2}) + \frac{1}{4}\cos^2\theta_{\text{spin}}] \tag{3}$$

where α is the angle between total momentum transfer $\mathbf{Q}$ and its out-of-plane component $\mathbf{Q}_{\perp}$. θ_{spin} is the angle between the spin and sample c-axis direction. In underdoped cuprates, it is assumed that $\theta_{\text{spin}} \approx 90°$. Then the polarization preserving elastic scattering amplitude becomes identical for the grazing-incidence ($\alpha < 0$) and grazing-exit ($\alpha > 0$) geometry with fixed $|\mathbf{Q}_{\parallel}|$.

From our RIXS data on LESCO and LSCO, we determine the ratio between charge order diffraction amplitude with σ and π polarized incident x-ray to be $I(\sigma,\sigma)/I(\pi,\pi) \approx 2.7$ [see Fig. 1(f)] and ≈ 2.8 [see Fig. S2(d)], respectively. These results are in good agreement with the theoretical value $I(\sigma,\sigma)/I(\pi,\pi) \approx 2.6$ calculated using Eq. (2) and (3). The scattering geometry dependence of the *dd*-excitation intensity is more complicated [4]. However, with all our experimental configurations, we estimate the variation of the integrated intensity of *dd* excitations to be within $\sim 20\%$. To account for this, an error of 20% is added when data are normalized across different instruments/polarizations.

Table S 1. Summary of RIXS experimental configurations.

Sample	$a \approx b$ (Å)	c (Å)	Beamline	σ_{G} (meV)	γ (°)	ℓ (r.l.u.)	ℓ_0 (r.l.u.)	Pol. (in)	Grazing in/exit	T (K)
LESCO	3.79	13.1	ADRESS	48	130	1.33–1.73	1.59	σ, π	exit	24–210
			I21	19	154	1.47–1.86	1.74	σ, π	exit	9–300
LNSCO	3.78	13.1	ADRESS	54	130	1.26–1.68	1.55	σ	in	16
LBCO	3.78	13.2	ID32	48	114–125	1.50	1.50	π	exit	20
LSCO	3.78	13.2	ADRESS	56	130	1.59	1.59	σ, π	exit	20

II. FITTING OF RIXS SPECTRA

The zero energy loss is determined by fitting the low-energy part of each RIXS spectrum. We describe the elastic scattering by a Gaussian profile where the width is set by the instrumental energy resolution (orange lines in Fig. S1). This energy resolution thus represents a technique-specific upper bound of the time scale below which fluctuations are considered as "static". The low-energy inelastic scattering is dominated by magnetic excitations. A damped harmonic oscillator is adopted to model the imaginary part of the spin dynamic susceptibility:

$$\chi''(\mathbf{Q},\omega) = \frac{\chi_0''}{2\omega_0}\left[\frac{\Gamma/2}{(\omega-\omega_0)^2+(\Gamma/2)^2} - \frac{\Gamma/2}{(\omega+\omega_0)^2+(\Gamma/2)^2}\right] \tag{4}$$

The corresponding RIXS intensity from magnetic scattering $S(\mathbf{Q},\omega)$ is given by:

$$S(\mathbf{Q},\omega) = \frac{\chi''(\mathbf{Q},\omega)}{1-e^{-\hbar\omega/k_{\mathrm{B}}T}} \tag{5}$$

where $\hbar$ is the reduced Planck constant and k_{B} is the Boltzmann constant. We have convoluted $S(\mathbf{Q},\omega)$ with the energy resolution function. The resulting profile is depicted by the green lines in Fig. S1. A quadratic function is added to mimic the background (BG). The quality of fitting can be appreciated in Fig. S1 and Fig. 2(f). The same analysis protocol was used in Ref. [5].

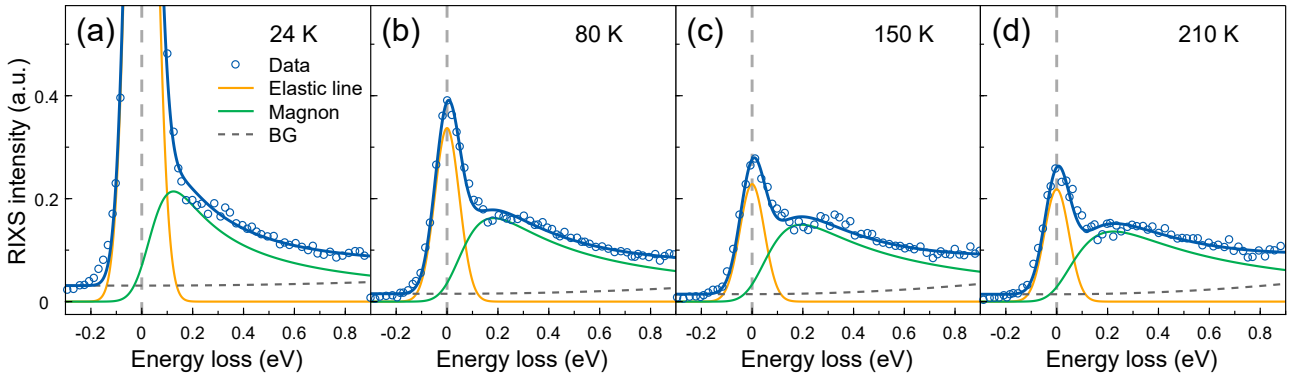

Figure S 1. **Raw RIXS spectra in LESCO.** Representative raw RIXS spectra at $\mathbf{Q}_{\mathrm{CO}}$ at (a) 24 K, (b) 80 K, (c) 150 K and (d) 210 K with fits and each fitted component.

III. RAW DATA, NORMALIZATION AND INTEGRATION OF DIFFRACTION INTENSITIES

Figs. S2(a)–S2(d) show representative raw data of the elastic **Q**-scans measured on LESCO, LNSCO, LBCO and LSCO, respectively. The **Q**-scans presented in the manuscript are obtained by subtracting linear backgrounds.

For a direct comparison between different samples, the charge order scattering intensities are normalized to the area of *dd* excitations. Data obtained with π polarization are given a geometric scaling factor according to the discussion in the previous section. The modulation of the charge order intensity $I(\ell)$ along ℓ, weak though, is also considered in the normalization using the relation $I(\ell) \propto \sin^2(\pi\ell)$ [6, 7]. The difference between the self-absorption coefficients for each experimental setup has been corrected following the procedure discussed in detail in the Supporting Information of Ref. [5]. In general, the self-absorption effect is minimized with grazing incidence geometry. This leads to an enhancement of raw elastic intensity in LNSCO where grazing incidence geometry was adopted [Fig. S2(b)]. The normalization processes are justified by the following facts. *(i)* The crystal field environments are similar across La-based single-layer cuprates. *(ii)* The energy window of elastic intensity integration is always set by the experimental energy resolution. Results on the same LESCO sample obtained at two instruments show good consistency [see Figs. 2(g), 2(h) and 3]. We have therefore normalized the I21 data to the ADRESS data by the peak amplitudes at the overlapping temperature (24–25 K). Charge order intensities in LBCO from Ref. [5] are normalized to the amplitude of *h*-scan at base temperature of this work. We note that in Ref. [5], two components are used to analyze the charge order peak in LBCO. To avoid complexity, in our analysis we have only included data from Ref. [5] measured below 40 K where the low-temperature component dominates charge order scattering intensity.

While charge orders in all La-1/8 compounds share roughly a constant in-plane integrated intensity (Fig. S3), their low-temperature diffraction peaks are found to be best described by different profiles: A Gaussian function is used to fit the longitudinal scans in LESCO and LNSCO [Figs. S2(a) and S2(b)]; a Lorentzian-squared function for the longitudinal scans in LBCO [Fig. S2(c) and Ref. [5]]; and a function comprising two Gaussians of equal width and height for the azimuthal scan (approximately along the transverse direction) in LSCO [Fig. S2(d)]. The correlation lengths extracted from these fittings are consistent with previous reports [5, 8, 9]. In LESCO, LNSCO and LBCO, the charge order peak is isotropic in the *hk*-plane [5, 10], while in LSCO it can be viewed as two split isotropic peaks [9].

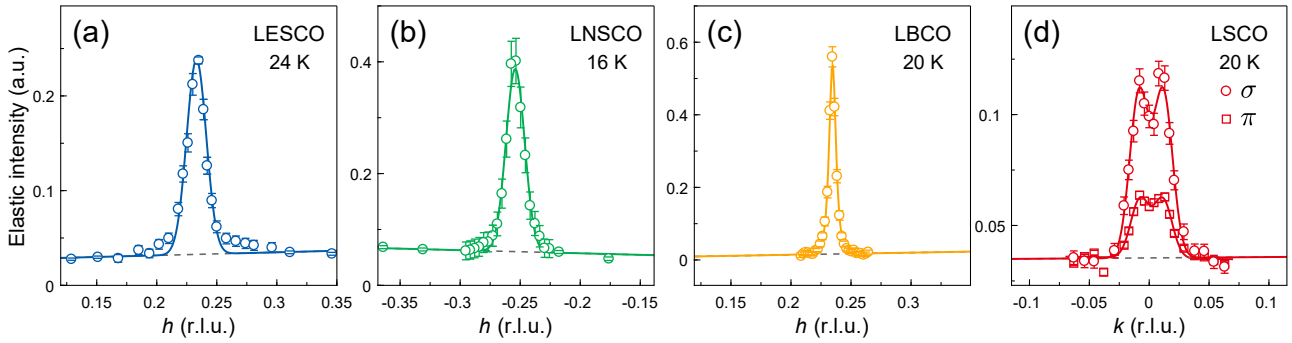

Figure S 2. Raw data of the elastic Q-scans through the charge order peak. (a), (b) Raw *h*-scans measured on (a) LESCO and (b) LNSCO with σ polarization. (c) Raw *h*-scan measured on LBCO with π polarization. (d) Raw azimuthal scans (ϕ-scans) measured on LSCO with both σ and π polarizations. The solid lines are fits to the raw data. The dashed lines indicate backgrounds. Error bars are three times the standard deviations. Data for LSCO with π polarization have been shifted vertically for clarity.

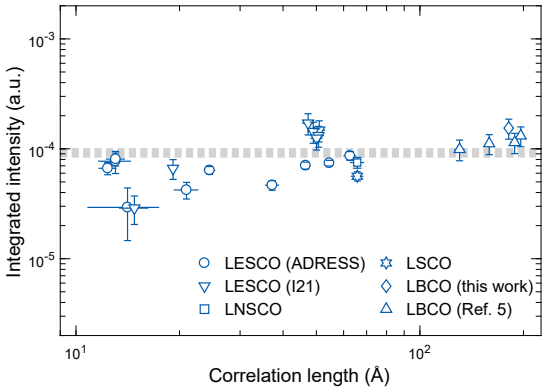

Figure S 3. In-plane integrated intensity of the charge order scattering versus correlation length for different La-1/8 compounds.

Based on these facts, we extend the peak profiles into their two-dimensional forms and calculate the peak volume as the in-plane integrated intensity of the charge order diffraction.

IV. ENERGY RESOLUTION OF THE RIXS SPECTROMETERS

We used spectra recorded on amorphous carbon tape to evaluate the energy resolution. Elastic scattering from the carbon tape overwhelms largely any inelastic component. It thus provides the most clear-cut extraction of the effective energy resolution. An example profile from the I21 instrument at the Diamond synchrotron is shown in Fig. S4. This profile is fitted to a Gaussian, Lorentzian and Voigt function, respectively. In this fashion, it is shown that the lineshape is predominately Gaussian. The additional fitting parameters included into the Voigt function, although improving the fitting of the low-intensity tail, do not lead to a significant correction to the evaluation of the energy resolution. In Table S1, we therefore parameterize the energy resolution by the Gaussian standard deviation. A Gaussian profile is also used for the fitting of elastic scattering in the spectra recorded on the stripe-ordered samples.

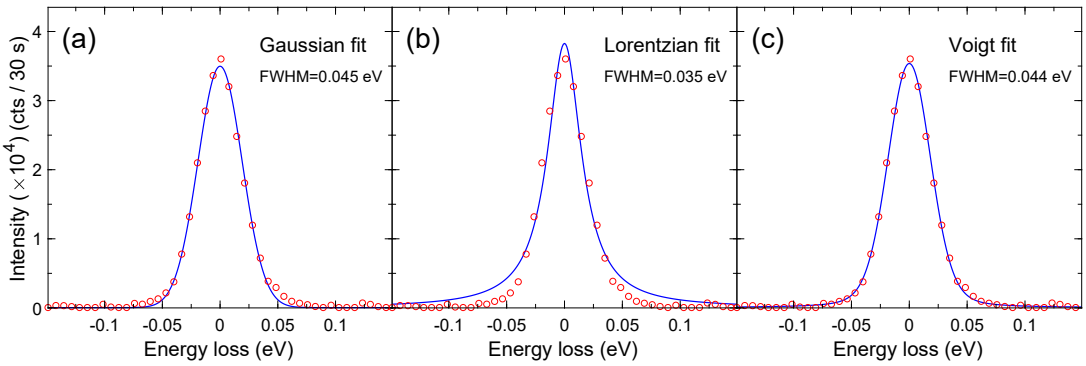

Figure S 4. RIXS spectrum recorded on amorphous carbon tape. (a)–(c) The same spectrum for which the elastic line is fitted to a Gaussian, Lorentzian and Voigt function, respectively. The profile is to a good approximation described by a Gaussian lineshape and naturally the additional fitting parameters included in the Voigt function lead to a further improvement.

V. TEMPERATURE DEPENDENCE OF INELASTIC SPECTRAL WEIGHT.

At base temperature, elastic scattering from the charge-stripe order largely dominates over the inelastic sector. With increasing temperature, this elastic signal weakens and eventually becomes comparable first to the *dd* excitations and ultimately to the response of spin excitations. It is therefore important to characterize the temperature dependence of the spin-excitation spectral weight. For illustration purpose, we are using data recorded at the ADRESS instrument with an energy resolution of $\sigma_{\mathrm{G}} \sim 48$ meV. In Fig. S5, we integrated the spin excitation spectral weight in the window of 200–500 meV. By being more than four Gaussian standard deviations away from the elastic line, the weight is surely dominated by inelastic processes. Notice that for $\mathbf{Q} = \mathbf{Q}_{\mathrm{CO}}$ this statement is only getting more accurate as temperature is increased. Whether being at $\mathbf{Q} = (0.235, 0)$ (near $\mathbf{Q}_{\mathrm{CO}}$) or at $\mathbf{Q} = (0.346, 0)$ (background), an approximate constant high-temperature tail is observed. Similar spectral weight conservation is expected from phonons. On this basis, we exclude that inelastic processes can be responsible for the decaying elastic intensity found at $\mathbf{Q}_{\mathrm{CO}}$.

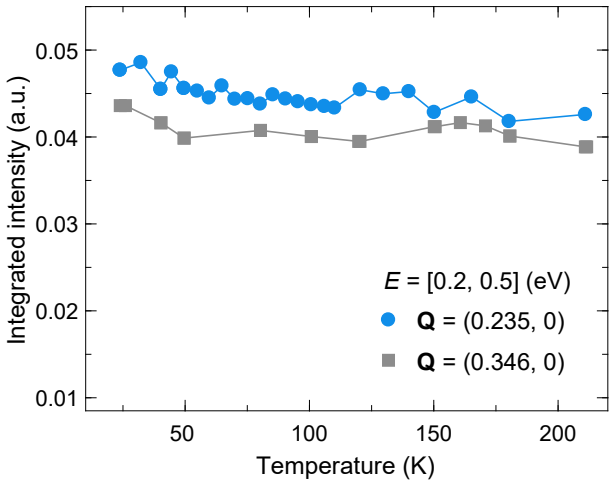

Figure S 5. Integrated inelastic spectral weight versus temperature. For $\mathbf{Q} = (0.235, 0)$ and $\mathbf{Q} = (0.346, 0)$, inelastic intensity is integrated in the window 200–500 meV. Overall only weak variations are found and in the temperature range 100–200 K, the intensity is approximately constant.

VI. TRANSITION FROM LTO TO LTT CRYSTAL STRUCTURE.

As in $La_{2-x}Ba_xCuO_4$ and $La_{1.6-x}Nd_{0.4}Sr_xCuO_4$, the $La_{1.8-x}Eu_{0.2}Sr_xCuO_4$ also undergoes a structural transition from low-temperature orthorhombic (LTO) to low-temperature tetragonal (LTT) structure. The highest transition temperature $\sim$ 125 K is found in the $La_{1.8-x}Eu_{0.2}Sr_xCuO_4$. Fig. 1(d) displays the $(3, 0, 0)$ Bragg peak – that is allowed in LTT phase but forbidden in the LTO structure – as a function of temperature. As expected, the amplitude of the $(3, 0, 0)$ Bragg peak drops to zero around the LTT to LTO transition. In Fig. S6, the $(2, 2, 0)$ Bragg peak is shown as a function of temperature. Above the structural transition, the $(2, 2, 0)$ Bragg peak is split due to the orthorhombicity. The orthorhombic splitting drops sharply to zero at the transition temperature. As there are no continuous connection between the lattice distortions in the LTO and LTT phase, the structural phase transition is

first order in agreement with our and published data [11, 12]. Since there is no evidence of a first order transition in the scattering amplitude from the charge order, there is no direct proportionality between the $(3, 0, 0)$ LTT Bragg peak and the stripe order in $La_{1.8-x}Eu_{0.2}Sr_xCuO_4$.

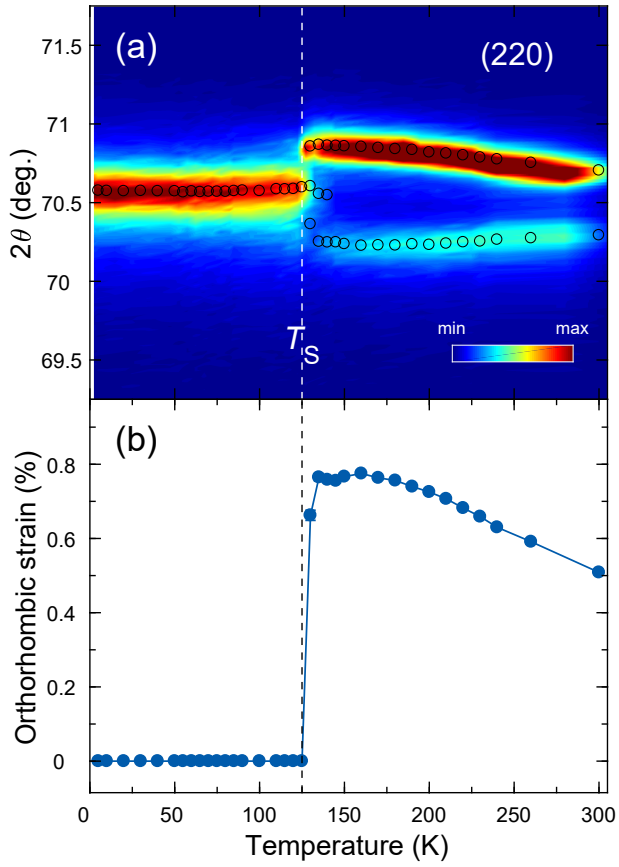

Figure S 6. LTO to LTT transition observed through the $(2, 2, 0)$ Bragg peak. (a) False color map of diffracted intensity versus temperature and scattering angle 2θ across the $(2, 2, 0)$ Bragg reflection. The open circles denote the peak positions fitted from the longitudinal scans. For consistency, notation in the HTT phase is used. (b) Orthorhombic order parameter – defined by $2(b_o - a_o)/(a_o + b_o)$ where a_o and b_o are the lattice constants in the orthorhombic phase – versus temperature.

[1] L. J. P. Ament, M. van Veenendaal, T. P. Devereaux, J. P. Hill, and J. van den Brink, Rev. Mod. Phys. **83**, 705 (2011).

[2] L. J. P. Ament, G. Ghiringhelli, M. M. Sala, L. Braicovich, and J. van den Brink, Phys. Rev. Lett. **103**, 117003 (2009).

[3] M. W. Haverkort, Phys. Rev. Lett. **105**, 167404 (2010).

[4] M. M. Sala, V. Bisogni, C. Aruta, G. Balestrino, H. Berger, N. B. Brookes, G. M. de Luca, D. D. Castro, M. Grioni, M. Guarise, P. G. Medaglia, F. M. Granozio, M. Minola, P. Perna, M. Radovic, M. Salluzzo, T. Schmitt, K. J. Zhou, L. Braicovich, and G. Ghiringhelli, New J. Phys. **13**, 043026 (2011).

[5] H. Miao, J. Lorenzana, G. Seibold, Y. Y. Peng, A. Amorese, F. Yakhou-Harris, K. Kummer, N. B. Brookes, R. M. Konik, V. Thampy, G. D. Gu, G. Ghiringhelli, L. Braicovich, and M. P. M. Dean, Proc. Natl. Acad. Sci. **114**, 12430 (2017).

[6] M. v. Zimmermann, A. Vigliante, T. Niemöller, N. Ichikawa, T. Frello, J. Madsen, P. Wochner, S. Uchida, N. H. Andersen, J. M. Tranquada, D. Gibbs, and J. R. Schneider, Europhys. Lett. **41**, 629 (1998).

[7] H. Kimura, H. Goka, M. Fujita, Y. Noda, K. Yamada, and N. Ikeda, Phys. Rev. B **67**, 140503(R) (2003).

[8] J. Kim, H. Zhang, G. D. Gu, and Y.-J. Kim, J. Supercond. Nov. Magn. **22**, 251 (2009).

[9] V. Thampy, M. P. M. Dean, N. B. Christensen, L. Steinke, Z. Islam, M. Oda, M. Ido, N. Momono, S. B. Wilkins, and J. P. Hill, Phys. Rev. B **90**, 100510(R) (2014).

[10] S. B. Wilkins, M. P. M. Dean, J. Fink, M. Hücker, J. Geck, V. Soltwisch, E. Schierle, E. Weschke, G. Gu, S. Uchida, N. Ichikawa, J. M. Tranquada, and J. P. Hill, Phys. Rev. B **84**, 195101 (2011).

[11] M. Hücker, M. v. Zimmermann, G. D. Gu, Z. J. Xu, J. S. Wen, G. Xu, H. J. Kang, A. Zheludev, and J. M. Tranquada, Phys. Rev. B **83**, 104506 (2011).

[12] B. Simovič, M. Hücker, P. C. Hammel, B. Büchner, U. Ammerahl, and A. Revcolevschi, Phys. Rev. B **67**, 224508 (2003).